

# Vectorial scale-based fuzzy-connected image segmentation

Ying Zhuge, Jayaram K. Udupa \*, Punam K. Saha

Medical Image Processing Group, Department of Radiology, University of Pennsylvania, Philadelphia, PA 19104, USA

Received 8 September 2004; accepted 15 July 2005

Available online 2 November 2005

## Abstract

This paper presents an extension of previously published theory and algorithms for fuzzy-connected image segmentation. In this approach, a strength of connectedness is assigned to every pair of image elements. This is done by finding the strongest among all possible connecting paths between the two elements in each pair. The strength assigned to a particular path is defined as the weakest affinity between successive pairs of elements along the path. Affinity specifies the degree to which elements hang together locally in the image. A scale is determined at every element in the image that indicates the size of the largest homogeneous hyperball region centered at the element. In determining affinity between any two elements, all elements within their scale regions are considered. This method has been effectively utilized in several medical applications. In this paper, we generalize this method from scalar images to vectorial images. In a vectorial image, scale is defined as the radius of the largest hyperball contained in the same homogeneous region under a predefined condition of homogeneity of the image vector field. Two different components of affinity, namely homogeneity-based affinity and object-feature-based affinity, are devised in a fully vectorial manner. The original relative fuzzy connectedness algorithm is utilized to delineate a specified object via a competing strategy among multiple objects. We have presented several studies to evaluate the performance of this method based on simulated MR images, 20 clinical MR images, and 250 mathematical phantom images. These studies indicate that the fully vectorial fuzzy connectedness formulation has generally overall better accuracy than the method using some intermediate ad hoc steps to fit the vectorial image to a scalar fuzzy connectedness formulation, and precision and efficiency are similar for these two methods.

© 2005 Published by Elsevier Inc.

**Keywords:** Fuzzy connectedness; Scale; Vectorial image; Image segmentation

## 1. Introduction

Multidimensional images are currently routinely available through sensing devices [1]. Research on defining objects in these image data—an activity generally referred to as image segmentation—spans over three decades [2]. There are many general frameworks proposed to deal with this problem. These may be broadly classified into *boundary-based*, *region-based*, and *hybrid* strategies.

*Boundary-based* approaches focus on delineating the interface between the object and the surrounding co-objects in the image. *Optimum boundary detection* approaches [3] attempt to automate boundary tracing, and pose

boundary delineation as an optimization problem. *Active contour or deformable boundary* methods [4,5] set up a mechanical system to deform an initial boundary specified somewhat close to the desired boundary. The final segmented boundary is taken to be that boundary for which an energy functional is minimized. These methods have been extended [6] to the color space, where object boundaries are obtained as a minimal “color weighted” path in a Riemannian space. A different family of user-steered delineation methods called *live-wire* have been developed [7,8], which detect optimal boundaries in a manner different from active contour methods. In these techniques, recognition by a human operator and delineation by the computer take place cooperatively, synergistically, and with a certain degree of continuity in a tightly coupled manner. *Active shape and appearance* methods [9,10] have emerged recently

\* Corresponding author. Fax: +1 215 898 9145.

E-mail address: [jay@mipg.upenn.edu](mailto:jay@mipg.upenn.edu) (J.K. Udupa).

in an attempt to overcome some of the inadequacies of the deformable boundary methods. These methods bring in constraints explicitly based on the shape of the boundary as well as on the intensity patterns in the vicinity of the boundary. Another class of boundary-based delineation techniques called *level-set* methods [11] have emerged also attempting to overcome the inadequacies of the deformable boundary methods. They can handle changing topology naturally, and can deal with local voxel level deformations.

*Region-based* approaches concentrate on delineating the region occupied by the object in the image. The simplest among region-based methods is intensity *thresholding*. Many methods to automatically find the thresholds in some optimum fashion have been devised [12,13]. *Region growing* methods [14] evolved in an attempt to overcome the drawbacks of thresholding. *Clustering or feature space partitioning* methods [15–17] are among the popular region-based delineation techniques. The basic premise of these methods is that object regions are manifest as clusters in an appropriate feature space, and therefore, to segment the object regions, we need to identify and delineate the clusters in the scatter plot defined in the feature space. A clustering-based approach for color image segmentation is proposed in [18], in which the number of classes and their center vectors are determined by a coarse segmentation; the unclassified pixels after the coarse segmentation are then assigned to the closest classes by using the fuzzy *c*-means (FCM) method. *Graph-based* approaches [19,20] to region delineation pose delineation as a graph problem and present a solution via graph search algorithms.

A variety of *Statistical model-based* methods are used which classify the image into different object classes in terms of the probability values, which are determined based on the intensity distribution of each class in the image. Parameters of the intensity distribution are usually estimated via the expectation-maximization (EM) algorithm. In the Bayesian method of [21], instead of a single multiplicative background intensity inhomogeneity that affects all tissue intensities, separate parametric smooth models are used for the intensity of each class. Then, a brain atlas is used in conjunction with a robust registration procedure to find a non-rigid transformation that maps the standard brain to the specimen to be segmented. This transformation is used to segment the brain from non-brain tissue, to compute prior probabilities for each class at each voxel location, and to find an appropriate automatic initialization. Finally, a variant of the EM algorithm is applied. A hidden Markov Random Field (MRF) [22] model with spatial information taken into account for segmentation of multispectral brain MR images is developed in [23]; the EM algorithm was also utilized for solving maximum likelihood estimation of model parameters. In [24], by means of MRF, non-parametric intensity distribution, neighborhood correlations, and inhomogeneities are combined in one segmentation algorithm. In [25], a statistical scheme for the segmentation of MR images in the presence of noise and intensity inhomogeneities is proposed. Noise

and inhomogeneities are explicitly incorporated into a Gaussian mixture model. The piecewise contiguous nature of the segmentation is modeled by a MRF. A greedy algorithm based on iterative conditional modes (ICM) is used to find an optimal segmentation while estimating the model parameters. An unsupervised Bayesian color image segmentation method is proposed in [26]. A first order MRF model is used where the singleton energies derived from a multivariate Gaussian distribution and second order potentials favor similar classes in neighboring pixels. The number of Gaussian mixture components is estimated by using reversible jump Markov chain Monte Carlo.

The *Watershed* family of methods is commonly used for region delineation [27]. In this approach, the  $n$ -dimensional image is considered as a surface in an  $(n + 1)$ -dimensional space. In the 2D image, the region occupied by an object in the image is considered to be the set of all those voxels which get flooded under certain conditions when the water level is gradually raised from a starting basin in the surface that corresponds to a set of seed voxels in the object in the image. A method of multiscale gradient watersheds for color image segmentation is presented in [28], which comprises of a non-linear scale-space with vector-valued gradient watersheds.

*Hybrid* approaches attempt to combine the strengths of both boundary-based and region-based approaches. These methods include approaches utilizing the results of region-based methods to assist in boundary finding [29,30], combining fuzzy connectedness with the deformable boundary strategy [31], and combining a voronoi-diagram method with a deformable boundary method [32], combining snakes, region growing, and Bayes/MDL for multiband image segmentation [33].

Fuzzy connectedness, which is the basis of the method proposed in the present paper, is a region-based segmentation framework developed in the 1990s. The premise behind this framework is the following. Images are by nature fuzzy. The spatial elements (spels) in an object region usually have a gradation of intensity values in an image. In spite of this graded composition of spel intensities, spels hang together to define an object in a global sense. This framework attempts to handle both these aspects in a fuzzy setting. Considerable progress has been made toward the goal of handling data inaccuracies by using fuzzy subset theory as a mathematical vehicle [34,35]. However, attempts to handle the notion of hanging togetherness also in the same fuzzy setting are sparse [36,37]. A framework of fuzzy-connected object definition theory and algorithms is proposed in [38]. In this framework, a local fuzzy relation called *affinity* is defined on the image domain, which assigns to every pair of nearby spels a strength of local hanging togetherness which has a value in  $[0,1]$ . Affinity between two spels depends on their spatial nearness as well as on how similar their image intensities and intensity-derived features are. A global fuzzy relation called *fuzzy connectedness* is defined on the image domain, which assigns to every pair  $(c,d)$  of spels a strength of global hanging

togetherness that has a value in  $[0, 1]$ . To determine this value, every possible path from  $c$  to  $d$  is considered and the minimum affinity of pairwise spels along the path is determined. This affinity represents the strength of this path. The strength of hanging togetherness (connectedness) between  $c$  and  $d$  is the largest of the strengths of all paths between  $c$  and  $d$ . An investigation on how to define affinity in practical image segmentation including a scale-based formulation of fuzzy connectedness is reported in [39]. By allowing object regions to compete in terms of connectedness strengths to win membership of elements, a relative fuzzy connectedness framework is developed in [40,41] which has been extended further in [42]. Improvement of the computational aspects of fuzzy connectedness is addressed in [43], its iterative extension is described in [41], and the case of multiple seeds is described in [44]. The fuzzy connectedness framework and its extensions have been effectively utilized in several medical applications. These include multiple sclerosis lesion detection and quantification via MR imaging [45], upper airway segmentation in children via MRI for studying obstructive sleep apnea [46], clutter-free volume rendering for MR angiography and artery–vein separation in MR angiography [47], automatic breast density estimation [48] via digitized mammograms for breast cancer risk assessment, and in brain tumor delineation via MR imaging [49]. Thousands of 3D images have been successfully processed so far, and, in some of these applications, the algorithms are in routine use in clinical trials. These experiences motivated us to further improve and extend this framework as proposed in this paper.

The aim of this work is to generalize the theory and algorithms of scale-based fuzzy connectedness from scalar images to vectorial images. The vectorial images may represent color images with R-, G-, and B-components, or multispectral images such as T1-, T2-, and PD-weighted images acquired via MR imaging. As noted in [50], the advantage of using MR images for 3D tissue segmentation is the multispectral characteristics of MR images with relaxation times (i.e., T1 and T2) and proton density (i.e., PD) information. Multispectral MR images provide more information than the individual images. Our desire to develop a fully vectorial fuzzy connectedness approach was based on the postulate that a fully vectorial formulation from the first principles, rather than some intermediate ad hoc steps to fit the images to a scalar fuzzy connectedness formulation, leads to more effective segmentations.

We present these generalizations in Section 2. Since the theoretical results generalize in a straightforward manner, we shall only state key results; the proofs follow directly from earlier publications. Where proofs deviate from the earlier results, they are given in the Appendix A. In Section 3, we present the associated algorithms. In Section 4, some examples drawn from several medical applications are presented and several evaluation studies are carried out to illustrate the behavior of the method. Our concluding remarks are stated in Section 5.

## 2. Theory

The terminology of [38] is followed throughout this paper. For completeness, some definitions are reproduced here from [38–40] to the extent they are needed for our discussion.

### 2.1. Fuzzy digital space, scenes, and binary scenes

Let  $Z$  denote the set of all integers. We use  $Z^n$  as the underlying digital grid, and the elements of  $Z^n$  will be called *spels* (short for spatial elements). When  $n = 2$ , spels are called pixels, and when  $n = 3$  they are called voxels. For any fuzzy subset or fuzzy relation  $X$ , we will use  $\mu_X$  to denote its membership function. A fuzzy relation  $\alpha$  in  $Z^n$  is said to be a *fuzzy spel adjacency* if it is reflexive and symmetric. The functional form of  $\mu_\alpha$  that we have used for the image processing results presented in this paper is as follows. For any spels  $c, d$ ,

$$\mu_\alpha(c, d) = \begin{cases} 1 & \text{if } c = d \text{ or } \|c - d\| \leq 1, \\ 0 & \text{otherwise,} \end{cases} \quad (2.1)$$

where  $\|c - d\|$  denotes the distance between  $c$  and  $d$ . The pair  $(Z^n, \alpha)$ , where  $\alpha$  is a fuzzy spel adjacency, will be referred to as a *fuzzy digital space*. A *vectorial scene* over a fuzzy digital space  $(Z^n, \alpha)$  is a pair  $\mathcal{C} = (C, \mathbf{f})$ , where  $C$  is a finite dimensional rectangular array of spels called the *domain* of  $\mathcal{C}$  and  $\mathbf{f} = (f_1, f_2, \dots, f_l)^T$  denotes a vector-valued *scene intensity function* whose domain is  $C$  and range is  $[L_1, H_1] \times [L_2, H_2] \times \dots \times [L_l, H_l]$ , where  $[L_i, H_i]$ , for  $1 \leq i \leq l$ , is the range of  $f_i$ ,  $L_i$ , and  $H_i$  being integers, and  $l$  is the vectorial dimension. We call  $\mathcal{C}$  a *binary scene* over  $(Z^n, \alpha)$  if  $\mathbf{f}$  is scalar valued and its range is  $\{0, 1\}$ . From now on, we assume that  $\mathcal{C} = (C, \mathbf{f})$  is the scene under consideration. For any set  $X$ , we use  $|X|$  to denote its cardinality.

### 2.2. Fuzzy spel affinity

Any fuzzy relation  $\kappa$  in  $C$  is said to be a *fuzzy spel affinity* (or, *affinity* for short) in  $\mathcal{C}$  if it is reflexive and symmetric. See [39] for the theory on construction of affinity relations especially with a scale-based formulation for the scalar case. The intent of  $\kappa$  is that  $\mu_\kappa(c, d)$  indicates the strength of local hanging-togetherness in the scene for any two spels  $c$  and  $d$  in  $C$  that are nearby. The concept of scale is used to define the neighborhood of  $c$  and  $d$  for affinity computation. Scale at any spel  $c$  is determined as the radius of the largest hyperball, centered at  $c$ , within which spel intensities are homogeneous. It is demonstrated in [39] that scale-based affinity is less sensitive to noise and still preserves fine details than the non-scale-based formulation. In [39], the following functional form is used for  $\mu_\kappa$ :

$$\mu_\kappa(c, d) = \mu_\alpha(c, d)g(\mu_{\phi_s}(c, d), \mu_{\psi_s}(c, d)), \quad (2.2)$$

where  $\psi_s$  and  $\phi_s$  represent homogeneity-based and object-feature-based components of affinity, respectively. The

strength of relation  $\psi_s$  indicates the degree of local hanging togetherness of spels because of their similarity of intensity values. The strength of  $\phi_s$  indicates the degree of local hanging togetherness of spels because of the agreement of their feature values to some expected object feature.  $g$  is any function that satisfies the following properties.

1. The range of  $g$  should be  $[0, 1]$ .
2.  $g$  should be such that for any given  $\mu_{\psi_s}$  (respectively,  $\mu_{\phi_s}$ ),  $\mu_{\kappa}$  should be monotonically non-decreasing with  $\mu_{\psi_s}$  (respectively,  $\mu_{\phi_s}$ ).

Roughly, it says that affinity should increase with each component. Several examples of  $g$  have been given in [39]. In this paper, we use the following form for  $g$ .

$$\mu_{\kappa} = \mu_{\alpha} \sqrt{\mu_{\psi_s} \mu_{\phi_s}}. \quad (2.3)$$

One of our aims in this paper is to generalize the above strategy from scalar to the vectorial case. We still think of  $\mu_{\kappa}$  to consist of a homogeneity-based component and an object-feature-based component, and denote them by  $\psi_{vs}$  and  $\phi_{vs}$ , respectively (“ $v$ ” denotes the vectorial case). The strength of affinity between any two nearby spels  $c$  and  $d$  is large when  $c$  and  $d$  are spatially close, the intensity vectors of spels in the vicinity of both  $c$  and  $d$  have a high degree of “homogeneity,” and the intensity vectors are close to an intensity vector expected for the object of interest. The extent of “vicinity” is determined by the scale values assigned to  $c$  and  $d$ . Scale, as in the scalar case [39], is a number assigned to every spel in the scene. It represents the radius of the largest hyperball centered at the spel within which the vectorial values of all spels are homogeneous. In determining affinity between two spels  $c$  and  $d$ , all spels within the hyperball associated with both spels are considered. In the rest of Section 2.2, we first describe how to estimate the scale value at every spel and then present the functional forms of  $\mu_{\psi_{vs}}$  and  $\mu_{\phi_{vs}}$ .

### 2.2.1. Scale estimation

For any  $c \in C$ , a hyperball  $B_k(c)$  of radius  $k$  centered at  $c$  is defined by

$$B_k(c) = \{e \in C \mid \|c - e\| \leq k\}. \quad (2.4)$$

We define a *fraction of object*  $FO_k(c)$  occupied by the region  $B_k(c) - B_{k-1}(c)$  which is sufficiently homogeneous with the intensity vector of  $c$  by

$$FO_k(c) = \frac{\sum_{d \in B_k(c) - B_{k-1}(c)} W_h(\mathbf{f}(d) - \mathbf{f}(c))}{|B_k(c) - B_{k-1}(c)|}, \quad (2.5)$$

where  $W_h$  is an unnormalized multivariate Gaussian homogeneity function

$$W_h(\mathbf{x}) = \exp(-\frac{1}{2}(\mathbf{x}^T \Sigma_h^{-1} \mathbf{x})), \quad (2.6)$$

where  $\Sigma_h$  is a homogeneity covariance matrix that indicates the co-variance among the different components of intensity that is allowed in order to still consider spels  $c$  and  $d$  as being homogeneous with each other.  $\Sigma_h$  can be estimated

over a homogeneous region of a given scene or over the entire given scene by excluding certain upper percentiles of gradients for accounting for edges. In Section 4.1, we shall give a detailed description on how to compute the parameters of  $\Sigma_h$ .

Scale at a spel  $c$  is estimated as the radius  $r(c)$  of the smallest hyperball for which  $FO_{r(c)}(c)$  falls below a tolerance limit  $\tau$ . In our experiments in this paper, we have used  $\tau = 0.85$  as recommended in [39] for the scalar case. The vectorial scale estimation algorithm is given below.

#### ALGORITHM VSE

**Input:**  $C, c \in C, W_h$ , a fixed threshold  $\tau$ .

**Output:**  $r(c)$ .

*begin*

set  $k = 1$ ;  
 while  $FO_k(c) \geq \tau$  do  
   set  $k$  to  $k + 1$ ;  
*endwhile*;  
 set  $r(c)$  to  $k$ ;  
 output  $r(c)$ ;

*end*

An example is shown in Fig. 1, wherein the object scale information (Fig. 1)B is shown as a 2D scene for the color vectorial scene of Fig. 1A. A zoomed in region of interest is also displayed. Note that, at tissue interfaces and at sites of fine and subtle features, the scale values are small (depicted darker), while they are large in the interior of large homogeneous regions (depicted brighter).

### 2.2.2. Homogeneity-based component of affinity ( $\psi_{vs}$ )

In determining scale-based fuzzy affinity between any spels  $c, d \in C$  such that  $\mu_{\alpha}(c, d) > 0$ , two digital hyperballs, centered at  $c$  and  $d$ , denoted  $B_{cd}(c)$  and  $B_{cd}(d)$ , both of radius  $\min[r(c), r(d)]$ , defined by

$$B_{cd}(c) = \{e \in C \mid \|c - e\| \leq \min[r(c), r(d)]\}, \quad (2.7)$$

$$B_{cd}(d) = \{e \in C \mid \|d - e\| \leq \min[r(c), r(d)]\}, \quad (2.8)$$

are used. Consider any spels  $e \in B_{cd}(c)$  and  $e' \in B_{cd}(d)$  such that they represent the corresponding spels within  $B_{cd}(c)$  and  $B_{cd}(d)$ . An effective inhomogeneity vector  $\mathbf{D}(c, d)$  among the spels in  $B_{cd}(c)$  and  $B_{cd}(d)$  is defined in the following manner:

$$\begin{aligned} \mathbf{D}(c, d) = & \sum_{\substack{e \in B_{cd}(c) \\ e' \in B_{cd}(d) \\ e-e'=c-d}} (1 - W_h(\mathbf{f}(e) - \mathbf{f}(e'))) \omega_{cd}(\|e - c\|) \\ & \times \frac{\mathbf{f}(e) - \mathbf{f}(e')}{\|\mathbf{f}(e) - \mathbf{f}(e')\|}, \end{aligned} \quad (2.9)$$

where  $\|\cdot\|$  yields the magnitude of a vector and  $\omega_{cd}$  is a zero-mean Gaussian distance weighting function whose standard deviation is  $\min[r(c), r(d)]$ .  $\mathbf{D}(c, d)$  represents the total unidirectional inhomogeneity over the scale regions around  $c$  and  $d$ . Homogeneity-based affinity  $\psi_{vs}$  is then defined by

$$\mu_{\psi_{vs}}(c, d) = 1 - \frac{|\mathbf{D}(c, d)|}{\sum_{e \in B_{cd}(c)} \omega_{cd}(\|e - c\|)}. \quad (2.10)$$



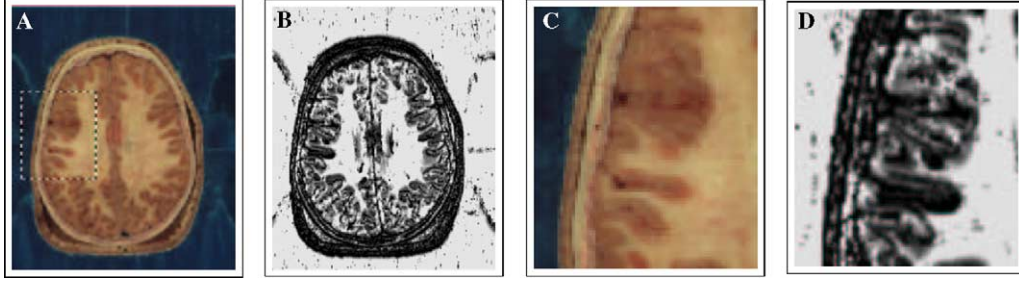


Fig. 1. (A) A slice from the Visible Human female color scene. (B) Estimated scale scene. (C) A closeup view for a region of interest selected in (A). (D) Corresponding view of scale scene for (C).

### 2.2.3. Object-feature-based component of affinity ( $\phi_{vs}$ )

For any spel  $c \in C$ , instead of using the vectorial value  $\mathbf{f}(c) = (f_1(c), f_2(c), \dots, f_l(c))^T$  to compute feature-value based agreement of belonging to an object of interest, a scale-based filtered version of  $\mathbf{f}(c)$  is considered. The filtered vectorial value at each spel  $c$  is denoted by  $\mathbf{f}_a(c) = (f_{a1}(c), f_{a2}(c), \dots, f_{al}(c))^T$ . Filtering is done simply by performing a weighted averaging of the vectors in the scale region of  $c$ .

$$\mathbf{f}_a(c) = \frac{\sum_{e \in B_r(c)} \omega_{cd}(\|c - e\|) \mathbf{f}(e)}{\sum_{e \in B_r(c)} \omega_{cd}(\|c - e\|)}, \quad (2.11)$$

where  $\omega_c$  is a zero mean Gaussian function with  $r(c)$  as the standard deviation parameter.

The object-feature-based affinity is then determined by

$$\mu_{\phi_{vs}}(c, d) = \begin{cases} 1 & \text{if } c = d, \\ \min[W_o(\mathbf{f}_a(c)), W_o(\mathbf{f}_a(d))] & \text{otherwise,} \end{cases} \quad (2.12)$$

where  $W_o(\mathbf{x})$  is a multivariate Gaussian function that expresses how close  $\mathbf{x}$  is to the expected feature vector for the object of interest

$$W_o(\mathbf{f}_a(c)) = \exp(-\frac{1}{2}(\mathbf{f}_a(c) - \mathbf{M}_o)^T \Sigma_o^{-1}(\mathbf{f}_a(c) - \mathbf{M}_o)), \quad (2.13)$$

and  $\mathbf{M}_o = (m_{o1}, m_{o2}, \dots, m_{ol})^T$  is the object mean intensity vector and  $\Sigma_o$  is the object intensity covariance matrix. These parameters are estimated over training sample regions as described in Section 4.1.

Finally, the vectorial scale-based affinity  $\kappa$  is defined by

$$\mu_{\kappa}(c, d) = \mu_z(c, d) \sqrt{\mu_{\psi_{vs}}(c, d) \mu_{\phi_{vs}}(c, d)}. \quad (2.14)$$

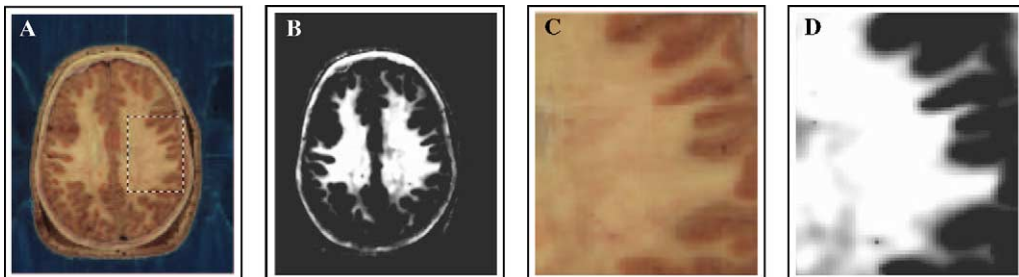


Fig. 2. (A) A slice from the Visible Human female color scene. (B) Computed affinity scene. (C) A closeup view for a region of interest selected in (A). (D) Corresponding view of affinity scene for (C).

Fig. 2 displays an example of the affinity relation determined for the Visible Human scene shown in Fig. 1. The affinity here is tailored to the white matter object. To display the affinity relation  $\kappa$  as a scene  $\mathcal{C}_{\kappa} = (C, f_{\kappa})$ , we have set, for any  $c \in C$ ,  $f_{\kappa}(c) = \frac{1}{3}(\sum_{i=1}^3 \mu_{\kappa}(c, d_i))$ , where  $d_i$ s are the spels for which  $\mu_{\kappa}(c, d_i) \neq 0$  (see (2.1)), and they are in the three positive co-ordinate directions with respect to  $c$ .

**Proposition 1.** For any vectorial scene  $\mathcal{C} = (C, \mathbf{f})$  over any fuzzy digital space  $(Z^n, \alpha)$ , the fuzzy relation  $\kappa$  whose membership function is  $\mu_{\kappa}$  as defined in (2.14) is a fuzzy spel affinity in  $\mathcal{C}$ .

### 2.3. Fuzzy $\kappa$ -connectedness and fuzzy objects

So far, we have discussed how local hanging togetherness of spels in terms of their vectorial characteristics can be formulated via spel affinity. In this section, we shall first derive the concept of global hanging togetherness of spels via fuzzy connectedness appealing to spel affinity. Subsequently, fuzzy connectedness will be utilized on its own to define an object in the scene (Section 2.3) and also in a competitive manner to define objects based on the relative strength of fuzzy connectedness in different objects (Section 2.4).

A path  $p_{cd}$  in  $\mathcal{C}$  from a spel  $c$  to a spel  $d$  is any sequence  $\langle c_1, c_2, \dots, c_q \rangle$ ,  $q \geq 2$ , of spels in  $C$  such that  $c_1 = c$  and  $c_q = d$ . The set of all paths in  $\mathcal{C}$  from  $c$  to  $d$  is denoted by  $P_{cd}$ . The set of all paths in  $\mathcal{C}$ , defined as  $\cup_{c,d \in C} P_{cd}$ , is denoted by  $P_C$ . The fuzzy  $\kappa$ -net  $\mathcal{N}_{\kappa}$  of  $\mathcal{C}$  is a fuzzy subset of  $P_C$  with its membership function defined as follows. For any path  $p_{cd} = \langle c = c_1, c_2, \dots, c_q = d \rangle \in P_C$ ,  $\mu_{\mathcal{N}_{\kappa}}(p_{cd}) = \min_{1 \leq i < q} [\mu_{\kappa}(c_i, c_{i+1})]$ . Vectorial fuzzy  $\kappa$ -connected-

ness in  $C$ , denoted  $K$ , is a fuzzy relation in  $C$ , defined as follows. For all  $c, d \in C$ ,

$$\mu_K(c, d) = \max_{p_{cd} \in P_{cd}} [\mu_{N_K}(p_{cd})]. \quad (2.15)$$

Similar to the scalar case, the similitude property holds for vectorial fuzzy  $\kappa$ -connectedness.

The Similitude property of a fuzzy relation is parallel to the equivalence property of a binary relation. In the scalar case, it has been shown that fuzzy connectedness is a similitude relation [38,44]. This property of fuzzy connectedness allows efficient computation, and also, it is essential to define an object (an equivalence class) at any specific strength. The following theorem states that, similar to the scalar case, the similitude property holds for vectorial fuzzy connectedness.

**Theorem 2.** For any vectorial scene  $\mathcal{C} = (C, \mathbf{f})$  over any fuzzy digital space  $(Z^n, \alpha)$ , vectorial fuzzy  $\kappa$ -connectedness  $K$  is a similitude relation.

Let  $\theta$  be any number in  $[0, 1]$ . A vectorial fuzzy  $\kappa\theta$ -object  $\mathcal{O}_{K\theta}(s)$  of  $\mathcal{C}$  containing a seed spel  $s$  of  $C$  is a fuzzy subset of  $C$  whose membership function is

$$\mu_{\mathcal{O}_{K\theta}(s)}(c) = \begin{cases} \eta(\mathbf{f}(c)) & \text{if } c \in \mathcal{O}_{K\theta}(s) \subset C, \\ 0 & \text{otherwise.} \end{cases} \quad (2.16)$$

In this expression,  $\eta$  is an objectness function whose domain is the range of  $\mathbf{f}$  and whose range is  $[0, 1]$ . It maps imaged scene intensity values into objectness values. For most segmentation purposes,  $\eta$  may be chosen to be a Gaussian whose mean and standard deviation represent the scene intensity distribution over the object region. The choice of  $\eta$  should depend on the particular imaging modality that generated  $\mathcal{C}$  and the actual physical object under consideration. In (2.16),  $\mathcal{O}_{K\theta}(s)$  is the support of  $\mathcal{O}_{K\theta}(s)$  which is a maximal subset of  $C$  such that it includes  $s$  and the strength of connectedness between any two of its spels is at least  $\theta$ . In other words,

$$(i) \ s \in \mathcal{O}_{K\theta}(s); \quad (2.17)$$

$$(ii) \text{ for any spels } c, d \in \mathcal{O}_{K\theta}(s), \mu_K(c, d) \geq \theta; \quad (2.18)$$

$$(iii) \text{ for any spel } c \in \mathcal{O}_{K\theta}(s) \text{ and any spel } d \notin \mathcal{O}_{K\theta}(s), \mu_K(c, d) < \theta. \quad (2.19)$$

A vectorial fuzzy  $\kappa\theta$ -object  $\mathcal{O}_{K\theta}(S)$  of  $\mathcal{C}$  containing a set  $S$  of seed spels of  $C$  is a fuzzy subset of  $C$  whose membership function is

$$\mu_{\mathcal{O}_{K\theta}(S)}(c) = \begin{cases} \eta(\mathbf{f}(c)) & \text{if } c \in \mathcal{O}_{K\theta}(S) = \bigcup_{s \in S} \mathcal{O}_{K\theta}(s), \\ 0 & \text{otherwise.} \end{cases} \quad (2.20)$$

We shall refer to  $\mathcal{O}_{K\theta}(S)$  as the support of  $\mathcal{O}_{K\theta}(S)$ .

**Theorem 3.** For any vectorial scene  $\mathcal{C} = (C, \mathbf{f})$  over  $(Z^n, \alpha)$ , for any fuzzy affinity  $\kappa$  in  $C$ , for any  $\theta \in [0, 1]$ , for any objectness function  $\eta$ , and for any non-empty set  $S \subset C$ , the support  $\mathcal{O}_{K\theta}(S)$  of the vectorial fuzzy  $\kappa\theta$ -object of  $\mathcal{C}$  containing  $S$  equals

$$\mathcal{O}_{K\theta}(S) = \{c | c \in C \text{ and } \max_{s \in S} [\mu_K(s, c)] \geq \theta\}. \quad (2.21)$$

As in the scalar case, the above theorem leads us to an efficient dynamic programming-based solution to the problem of defining a fuzzy-connected object in any vectorial scene, as described in the next section. The following important properties of fuzzy connectedness are satisfied by vectorial scenes also, whose proofs follow directly from the results for the scalar case [38–40].

As it is widely argued, a segmentation task must fulfill both recognition: location of the whereabouts of an object, and delineation: classification of each spel in a scene. In fuzzy connectedness, recognition is accomplished by specifying the seed spels. Although, human observers are superior to machines in fulfilling the recognition task, it is unrealistic to expect two observers (or, even one observer at two different time instants) to indicate seed spels at exact same locations. Therefore, fuzzy connectedness must behave robustly with respect to intra- and inter-operator variations in seed specification to achieve high reproducibility in segmentation results. The following theorem states the robustness property of vectorial fuzzy connectedness with respect to seed specification. Also, Proposition 5 states the behavior of the method as the connectivity threshold is changed while Proposition 6 states its behavior as some seed spels are dropped or a few more seed spels are added. Finally, Proposition 7 affirms the necessary and sufficient condition for hard connectivity of a fuzzy-connected object.

**Theorem 4.** For any vectorial scene  $\mathcal{C} = (C, \mathbf{f})$  over  $(Z^n, \alpha)$ , for any affinity  $\kappa$  in  $C$ , for any  $\theta \in [0, 1]$ , for any objectness function  $\eta$ , and for any non-empty sets  $S_1, S_2 \subset C$ ,  $\mathcal{O}_{K\theta}(S_1) = \mathcal{O}_{K\theta}(S_2)$  if and only if  $S_1 \subset \mathcal{O}_{K\theta}(S_2)$  and  $S_2 \subset \mathcal{O}_{K\theta}(S_1)$ .

**Proposition 5.** For any vectorial scene  $\mathcal{C} = (C, \mathbf{f})$  over  $(Z^n, \alpha)$ , for any affinity  $\kappa$  in  $C$ , for any  $\theta_1, \theta_2 \in [0, 1]$ , for any objectness function  $\eta$ , and for any non-empty set  $S \subset C$ ,  $\mathcal{O}_{K\theta_1}(S) \subset \mathcal{O}_{K\theta_2}(S)$  if  $\theta_2 < \theta_1$ .

**Proposition 6.** For any vectorial scene  $\mathcal{C} = (C, \mathbf{f})$  over  $(Z^n, \alpha)$ , for any affinity  $\kappa$  in  $C$ , for any  $\theta \in [0, 1]$ , for any objectness function  $\eta$ , and for any non-empty sets  $S_1, S_2 \subset C$ ,  $\mathcal{O}_{K\theta}(S_1) \subset \mathcal{O}_{K\theta}(S_2)$  if  $S_1 \subset S_2$ .

**Proposition 7.** For any vectorial scene  $\mathcal{C} = (C, \mathbf{f})$  over  $(Z^n, \alpha)$ , for any affinity  $\kappa$  in  $C$ , for any  $\theta \in [0, 1]$ , for any objectness function  $\eta$ , and for any non-empty set  $S \subset C$ , and for any spels  $c, d \in \mathcal{O}_{K\theta}(S)$ , all spels in the strongest path from  $c$  to  $d$  in  $C$  are contained in  $\mathcal{O}_{K\theta}(S)$  if and only if  $\min_{s_1, s_2 \in S} [\mu_K(s_1, s_2)] \geq \theta$ .

Proofs of the above theorem and propositions follow directly from the results for the scalar case [38–40].

#### 2.4. Relative vectorial fuzzy connectedness of multiple objects

Instead of defining an object on its own based on the strength of connectedness as done in Section 2.3 above, all other objects (co-objects) of importance that are present in the scene are also considered, and all objects are let to compete among themselves in having spels as their members in relative fuzzy connectedness [40]. In this competition, every pair of spels in the scene will have a strength of connectedness in each object. The object in which this strength is highest will claim membership of the spels. This approach of fuzzy object definition using relative strengths of connectedness eliminates the need for the threshold  $\theta$  of strength of connectedness that is part of the definition described above. All specified objects are defined simultaneously in this approach.

Let  $\mathcal{C} = (C, \mathbf{f})$  be any given vectorial scene over a fuzzy digital space  $(Z^n, \alpha)$ , which has information about  $m \geq 2$  objects, denoted  $O_1, O_2, \dots, O_m$ , captured in it through an image acquisition process. Let  $S_1, S_2, \dots, S_m$  denote sets of seed spels in  $C$  where  $S_i$  is specified for the object region  $O_i$ . Let  $\mathbf{S}$  denote the set  $\{S_1, S_2, \dots, S_m\}$  of the sets of seed spels. For any  $S \in \mathbf{S}$ , we shall use  $b(S)$  to denote  $(\cup_{S' \in \mathbf{S}, S' \neq S} S') - S$ , the idea being that  $b(S)$  denotes the set of reference spels chosen in the regions constituting the background as far as the object to which the spels of  $S$  belong is concerned.

For any  $S \in \mathbf{S}$ , we define

$$P_{Sb(S)_\kappa} = \{c | c \in C \text{ and } \max_{s \in S} \mu_\kappa(s, c) > \max_{s' \in b(S)} \mu_\kappa(s', c)\}. \quad (2.22)$$

A vectorial fuzzy  $\kappa$ -object  $\mathcal{O}$  of  $\mathcal{C}$  containing the set of spels  $S$  relative to a background (co-objects) containing the set of spels in  $b(S)$  is the fuzzy subset of  $C$  defined by the following membership function. For any  $c \in C$ ,

$$\mu_{\mathcal{O}_{Sb(S)_\kappa}}(c) = \begin{cases} \eta(\mathbf{f}(c)) & \text{if } c \in P_{Sb(S)_\kappa}, \\ 0 & \text{otherwise.} \end{cases} \quad (2.23)$$

As mentioned previously, our aim here is to compute the support region for each object and therefore, we use  $\eta(\mathbf{f}(c)) = 1$ . It is important that  $S_i \cap S_j$  be empty for all  $i \neq j$ ; otherwise, the intuitively desirable property that  $S \subset P_{ob(S)_\kappa}$  is not guaranteed. Similar to the case of scalar scenes and the case of one seed spel per object region, discussed in [44], the following property is satisfied for relative vectorial fuzzy connectedness with multiple seeds per object region. The proof follows along similar lines as described in [40].

**Proposition 8.** For any vectorial scene  $\mathcal{C} = (C, \mathbf{f})$  over  $(Z^n, \alpha)$ , for any affinity  $\kappa$  in  $C$ , and for any sets of spels  $S$  and  $S'$  in  $\mathbf{S}$  such that  $S \cap S' = \emptyset$  (the empty set),

$$P_{Sb(S)_\kappa} \cap P_{S'b(S')_\kappa} = \emptyset. \quad (2.24)$$

It is important to note that, in our theoretical descriptions, we confined ourselves to single affinity for different objects. Indeed, single affinity is a necessary condition for the prop-

erty (Proposition 8) of relative vectorial fuzzy connectedness to hold. However, in many applications, different object regions possess different intensity characteristics, and therefore, to optimally utilize scene information, it is desirable to use different affinities for different objects. Here, we describe how different object-oriented affinities may be combined into a single affinity. Let  $\kappa_1, \kappa_2, \dots, \kappa_m$  be affinities specified for the  $m$  object regions, respectively. These affinities may be combined into a single affinity  $\kappa$  that retains as much as possible the individual object-specific information [40]. In this paper, we use the fuzzy union of the individual affinities. That is,

$$\kappa = \bigcup_i \kappa_i. \quad (2.25)$$

### 3. Algorithm

In this section, we present an algorithm, called  $\kappa$ VSR-FOE (vectorial scale-based relative fuzzy object extraction), for extracting a vectorial relative fuzzy  $\kappa$ -object from a given scene  $\mathcal{C} = (C, \mathbf{f})$  containing a set  $S$  of seed spels of  $C$  relative to a background (co-objects) containing the set of spels in  $b(S)$ . For any spel affinity  $\kappa$  in a vectorial scene  $\mathcal{C} = (C, \mathbf{f})$  over a fuzzy digital space  $(Z^n, \alpha)$ , we define the  $\kappa$ -connectivity scene  $\mathcal{C}_{KS}$  of  $\mathcal{C}$  generated by the set  $S$  by  $\mathcal{C}_{KS} = (C, f_{KS})$ , where, for any  $c \in C$ ,  $f_{KS}(c) = \max_{s \in S} [\mu_\kappa(s, c)]$ .

Algorithm  $\kappa$ VSRFOE

**Input:**  $\mathcal{C} = (C, \mathbf{f})$ ,  $\eta$ ,  $\kappa$  as defined in Section 2, a set of the sets of seed spels  $\mathbf{S} = \{S_1, S_2, \dots, S_m\}$ , and a set  $S \in \mathbf{S}$ .

**Output:** A vectorial fuzzy  $\kappa$ -object  $\mathcal{O}$  of  $\mathcal{C}$  containing the set of spels  $S$  relative to a background (co-objects) containing the set of spels in  $b(S)$ .

**Auxiliary Data Structures:** The  $\kappa$ -connectivity scene  $\mathcal{C}_{KS_i} = (C, f_{KS_i})$  of  $S_i$  in  $\mathcal{C}$  for each  $S_i \in \mathbf{S}$ ; and a queue  $Q$  containing spels to be processed.

begin

```

0  for each  $S_i \in \mathbf{S}$  do
1    set  $f_{KS_i}(c) = 0$  for all  $c \in C$  except for all  $x \in S_i$ 
    set  $f_{KS_i}(x) = 1$ ;
2    push all  $x \in S_i$  to  $Q$ ;
3    while  $Q$  is not empty do
4      remove a spel  $c$  from  $Q$  for which  $f_{KS_i}(c)$  is
        maximal;
5      for each spel  $d$  such that  $\mu_\kappa(c, d) > 0$  do
6        set  $f_{\min} = \min(f_{KS_i}(c), \mu_\kappa(c, d))$ ;
7        if  $f_{\min} > f_{KS_i}(d)$  then
8          set  $f_{KS_i}(d) = f_{\min}$ ;
9          if  $d$  is already in  $Q$  then
10           update the location of  $d$  in  $Q$ ;
11          else push  $d$  to  $Q$ ;
```

```

12         endif;
13     endif;
14 endfor;
15 endwhile;
16 endfor;
17 for all  $c \in C$  do
18     if  $f_{KS}(c) > f_{KS_i}(c)$  for all  $S_i \in b(S)$  then
19         set  $\mu_O(c) = \eta(\mathbf{f}(c))$ ;
20     else set  $\mu_O(c) = 0$ ;
21     endif;
22 endfor;
23 output  $\mathcal{O}$ ;
end

```

In the above algorithm, Steps 0–16 are for computing the connectivity scenes  $\mathcal{C}_{KS_i}$  for all  $S_i \in \mathbf{S}$ . As shown previously, there are many efficient ways to compute connectivity scenes [43]. Here, we use the dial's implementation of Dijkstra's shortest path algorithm, which has been shown [43] to lead to the fastest strategy among a set of 18 algorithms. The data structure  $\mathcal{Q}$  are devised as a hashing heap, and we use the temporary connectedness strength (in our implementation, we transform the strength value between  $[0, 1]$  to an unsigned short value between  $[0, 4096)$ ) as a hashing key. Each item in the heap points to a doubly linked list in such a way that all nodes in the list have the same connectedness strength. For details, see [43]. The operations in Steps 4, 10, and 11 are carried out quite inexpensively by such an implementation. At the end of Step 16,  $\kappa$ VSRFOE produces the  $m$  connectivity scenes  $\mathcal{C}_{KS_i}$ ,  $1 \leq i \leq m$ . Steps 17–23 compute a particular relative fuzzy  $\kappa$ -object from these  $m$  scenes. Clearly, by repeating these steps, each of the  $m$  relative fuzzy  $\kappa$ -objects can be computed and output.

That this algorithm terminates and that at that time it indeed outputs the fuzzy  $\kappa$ -object  $\mathcal{O}$  of  $\mathcal{C}$  containing the set of spels  $S$  relative to the background co-objects containing the set of spels in  $b(S)$  follows from the proof of a similar algorithm for the scalar case [40].

#### 4. Results, evaluation, and discussion

In Section 4.1, we describe how the parameters of  $\psi_{vs}$  and  $\phi_{vs}$  are estimated. In Section 4.2, we briefly explain the inhomogeneity correction method used in our experiments. In Section 4.3, we present several examples to illustrate the behavior of the algorithm. We will present an evaluation of  $\kappa$ VSRFOE by using the framework of [51] in Section 4.4, and compare this with the scalar version of the relative fuzzy connectedness algorithm described in [52] in Section 4.5.

##### 4.1. Parameter estimation

In [39], parameters used in  $\psi_s$  and  $\phi_s$  were estimated over sample regions specified manually by operators. In

this paper, the homogeneity-based covariance matrix  $\Sigma_h$  is estimated from the entire scene by excluding certain upper percentiles of gradients which account for edges. This method produces more accurate parameters than those estimated from specified sample regions. The method to account for edges is as follows.

Let  $\mathcal{C} = (C, \mathbf{f})$  be a vectorial scene over  $(Z^n, \alpha)$ . For any spels  $c, d \in C$  satisfying (2.1), for each vector component  $i$  ( $1 \leq i \leq l$ ), we compute the histogram  $h_i(x)$ ,  $x \in [0, H_i - L_i]$  of  $|f_i(c) - f_i(d)|$ . Let  $F_i$  be the smallest integer in  $[0, H_i - L_i]$  such that

$$\frac{\sum_{j=0}^{F_i} h_i(j)}{\sum_{j=0}^{H_i-L_i} h_i(j)} \times 100 \geq \lambda, \quad (4.1)$$

where  $\lambda$  is a percentile value. In all our examples, we have used  $\lambda = 90$ . The homogeneity covariance matrix  $\Sigma_h$  is then estimated as follows:

$$\Sigma_{h_{ij}} = \frac{\sum_{\substack{c,d \in C \\ |f_i(c)-f_i(d)| < F_i \\ |f_j(c)-f_j(d)| < F_j}} \mu_x(c,d)(f_i(c) - f_i(d))(f_j(c) - f_j(d))}{\sum_{\substack{c,d \in C \\ |f_i(c)-f_i(d)| < F_i \\ |f_j(c)-f_j(d)| < F_j}} \mu_x(c,d)}, \quad (4.2)$$

$1 \leq i, j \leq l.$

To estimate the parameters of the relation  $\phi_{vs}$ , an operator paints a training region  $R$  for each object of interest on a display of one or more slices of the scene by using a mouse-controlled brush. The mean vector  $\mathbf{M}_o = (m_{o1}, m_{o2}, \dots, m_{ol})^T$  and object-feature covariance matrix  $\Sigma_o$  for each object are then estimated as follows:

$$m_{oi} = \frac{\sum_{c \in R} f_i(c)}{|R|}, \quad 1 \leq i \leq l, \quad (4.3)$$

where  $|R|$  represents the number of spels in region  $R$ , and

$$\Sigma_{o_{ij}} = \frac{\sum_{c \in R} (f_i(c) - m_{oi})(f_j(c) - m_{oj})}{|R|}, \quad 1 \leq i, j \leq l. \quad (4.4)$$

We note that the parameters of  $\phi_{vs}$  are estimated from training initially on one (or more) scene(s) and subsequently fixed for all scenes to be segmented for that application domain. Therefore, per scene training (and hence operator time) is not needed during segmentation.

##### 4.2. Inhomogeneity correction

In our experiments, all MRI data are first corrected. We utilize a general, entirely image-based strategy for correcting this variation [53]. The method is automatic, acquisition-protocol-independent, and requires no prior knowledge. A brief description of this method is given below.

The scale information is utilized to estimate homogeneous regions. Regions (balls) corresponding to the largest scale values in the foreground of the scene are first identified, and then the scene is thresholded by using intensity



intervals estimated from these regions. A 2nd order polynomial function is then fit to the intensity variation within the thresholded region, and inhomogeneity correction is effected by utilizing this polynomial. The process is iteratively repeated on the resulting scene until the changes found in two successive iterations are sufficiently small. In place of this method, any other correction strategy [54] can be utilized from the viewpoint of the main thrust of this paper.

#### 4.3. Examples

Information about the scene data used in our examples is shown in Table 1. In all these examples, we are interested in the intracranial brain tissues. Algorithm  $\kappa$ FOE of [38] and some morphological operations are utilized to extract the intracranial brain mask first. Then algorithm  $\kappa$ VSR-FOE is applied within the extracted brain mask to separate the tissues.

The first example, illustrated in Fig. 3, pertains to the Visible Human female color data set. The R-, G-, and B-components of one slice of the color scene representing part of the head are shown in Figs. 3A–C, respectively.

Table 1  
Information about scene data utilized as examples

Example	Protocol	Scene domain	Voxel size (mm <sup>3</sup> )
1	Color photograph	570 × 670 × 60	0.33 × 0.33 × 0.33
2	FSE $T_2$ , PD	256 × 256 × 53	0.86 × 0.86 × 3.0
3	FSE $T_2$ , PD	256 × 256 × 50	0.86 × 0.86 × 3.0

The segmented white and gray matter objects are shown as binary scenes in Figs. 3D and E, respectively.

Our second example, illustrated in Fig. 4, comes from MRI of the head of a clinically normal human subject. A fast-spin-echo dual-echo protocol is used to yield a 2-component vectorial scene. One slice of the PD and the  $T_2$  scenes is shown in Figs. 4A and B, respectively. The slices of the segmented 3D binary scene for gray matter (GM), white matter (WM), and cerebrospinal fluid (CSF) are also shown in the figure.

Our third example is shown in Fig. 5, which is an MRI scene of the head of a patient with Multiple Sclerosis (MS). In this instance, after the white and gray matter were separated, the lesions were selected and separated within the white matter by using a strategy similar to that in [45] but by employing vectorial scale-based relative fuzzy connectedness instead of the scalar non-scale-based absolute fuzzy connectedness method of [45].

#### 4.4. Evaluation

We use the framework described in [51] for evaluating the effectiveness of the proposed segmentation algorithm. In this framework, a method's performance is assessed by three sets of measures—precision, accuracy, and efficiency. Precision here refers to reliability of the method taking into consideration any subjective actions required in the method. Accuracy refers to how well the result agrees with true segmentation, and efficiency indicates the computational and operator time required in the segmentation process. The measures that are used under each of these groups

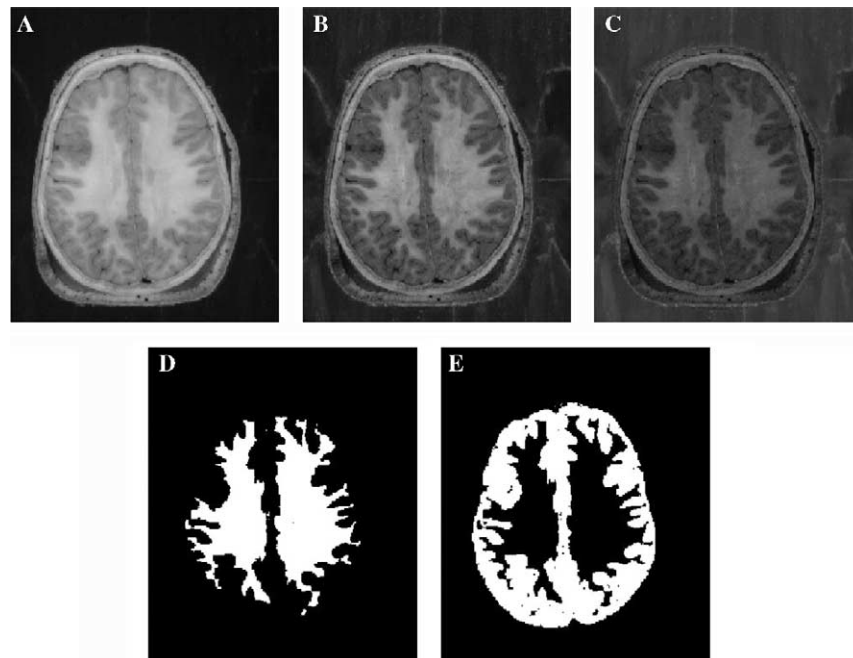


Fig. 3. (A–C) R-, G-, and B-components, respectively, of one slice of the Visible Human female color scene of the head. (D) Segmented white matter. (E) Segmented gray matter.

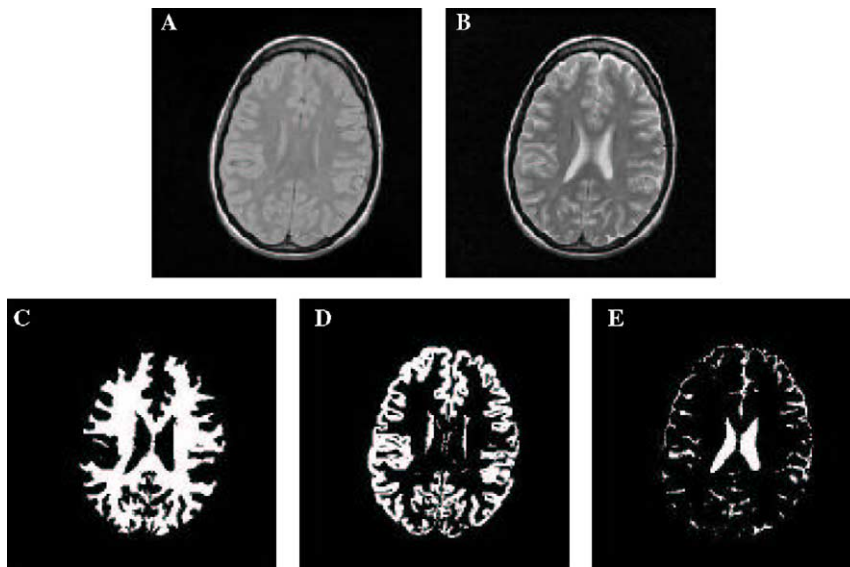


Fig. 4. (A) One slice of PD-weighted MRI scene of the head of a normal human subject. (B) Corresponding  $T_2$ -weighted MR slice. (C) Segmented white matter. (D) Segmented gray matter. (E) Segmented CSF.

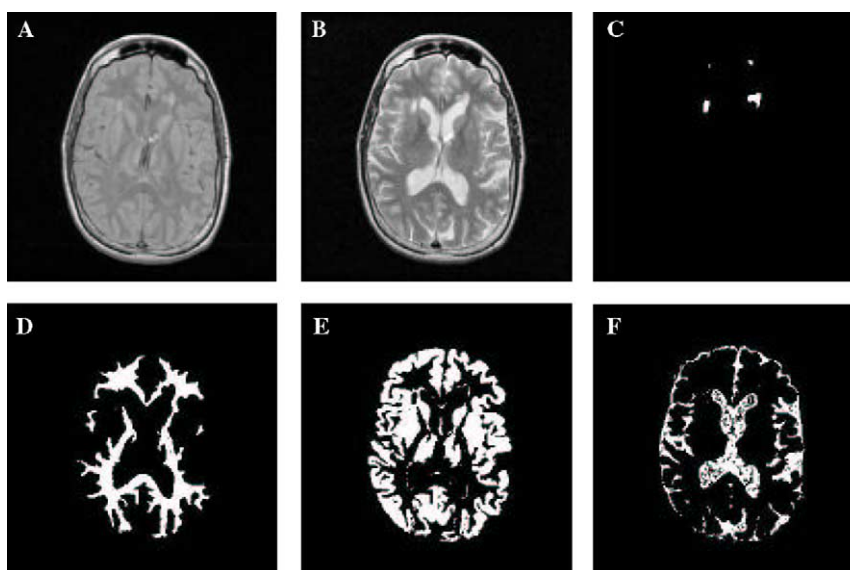


Fig. 5. (A) One slice of a PD-weighted MRI scene of the head of a patient with Multiple Sclerosis. (B) Corresponding  $T_2$ -weighted MR slice. (C) Segmented MS lesions. (D) Segmented white matter. (E) Segmented gray matter. (F) Segmented CSF.

and their definitions are given under the following subsections.

We performed two sets of evaluation experiments—one on simulated MRI scenes and the other on clinical MRI scenes. In the first set, we used the simulated MRI scenes of the head generated by using the BrainWeb MR simulator [55]. Simulated  $T_1$ ,  $T_2$ , and PD-weighted normal brain data sets with 1–7% noise and 0–40% inhomogeneity are utilized in our experiments. The volumes had the resolution of  $181 \times 217 \times 60$ , pixel size of  $1.0 \text{ mm} \times 1.0 \text{ mm}$ , slice thickness of 3.0 mm, 16-bit quantization. Since there is only one simulated data set corresponding to one brain for each of three protocols and no repeat scans are available, we evaluate only the accuracy measure. In the second

set, clinical scene data used in our evaluation experiments consist of 10 different MS patients and 10 normal subjects and are acquired with fast-spin-echo dual-echo PD- and  $T_2$ -weighted studies. These data sets were randomly selected from our database that contains about 100 patients with about 4000 3D scenes comprising different routinely applied MRI protocols, and acquired on the same GE Signa 1.5 T scanner with a quadrature transmitter/receiver head coil and consisted of contiguous axial slices covering the entire brain with a scene domain of  $256 \times 256 \times 56$ , pixel size of  $0.86 \text{ mm} \times 0.86 \text{ mm}$ , slice thickness of 3.0 mm, and FOV of 22 cm, with TR of 2500 ms and TE of 18 ms/90 ms. Two repeated scans were obtained for each patient with a short time gap in between scans during which the

patients were removed from the scanning table and then positioned again. This is for assessing the precision of the method with respect to patient positioning in the scanner. All these data sets have been first corrected for inhomogeneity by using the method described in [53] and subsequently intensity standardized by using the method of [56] before applying a segmentation method on them. For convenience of evaluation, we consider three tissue groups: WM, GM, and CSF. We have not treated MS lesions and abnormal WM as separate objects since it is very difficult to delineate them manually in a reliable manner because of their diffuse nature; they have been segmented as part of WM or GM. “True” segmentations of all objects have been obtained by carefully correcting the result of our algorithm segmentation under the guidance of an expert.

#### 4.4.1. Precision

Three factors are measured in evaluating segmentation precision—intra-operator precision  $PR^{T_1}$ , inter-operator precision  $PR^{T_2}$ , and repeat-scan precision  $PR^{T_3}$ . Let  $C_{O_1}$  and  $C_{O_2}$  be segmentations of the same object in two repeated trials. For inter- and intra-operator precision, we use the following definition to measure the overlap agreement.

$$PR^{T_i}(O_1, O_2) = \frac{|C_{O_1} \cap C_{O_2}|}{|C_{O_1} \cup C_{O_2}|}, \quad 1 \leq i \leq 2, \quad (4.5)$$

where  $\cap$  and  $\cup$  represent binary scene intersection and union operations, respectively, and  $|X|$  denotes the number of spels in binary scene  $X$  with value 1 assigned to them. For repeat scan precision, such an overlap measure cannot be made without scene registration. To avoid the error arising from registration and subsequently interpolation that is required to measure overlap, and this error influencing the precision measures, we measure the volume agreement of two repeated trials by

$$PR^{T_3}(O_1, O_2) = 1 - \frac{||C_{O_1}| - |C_{O_2}||}{\frac{1}{2}(|C_{O_1}| + |C_{O_2}|)}. \quad (4.6)$$

Table 2 shows intra-, inter-operator, and repeat-scan precision for segmenting WM, GM, and CSF by using our method over the 20 clinical scene data sets. Mean and standard deviation over the scene population are listed. Here, intra- and inter-operator precision (measured by two

operators specifying the seeds needed for WM, GM, and CSF two times on different occasions for the scenes involved in evaluation and by utilizing (4.5)) are 100%. This level of robustness stems mainly from MRI scene inhomogeneity correction and intensity standardization. We just need one time training to estimate parameters and fix them for all segmentation tasks. Thus, only the seeds for two repeat trials are different. Further, according to Theorem 4 and [41,44], any subset of spels selected in the support of the same fuzzy-connected object as seeds would generate the same fuzzy connectedness object upon segmentation. The slightly lower values of repeat-scan precision are understandable because of the sensitivity of the different ways in which fine and thin aspects of the three objects, especially peripheral CSF, are digitized because of change in patient orientation.

#### 4.4.2. Accuracy

For any scene  $C = (C, f)$ , let  $C_O$  be the segmentation result (binary scene) output by a segmentation method for which the true (surrogate) delineation result is  $C_{td}$ . Then the two measures of accuracy recommended in [51], namely, FPVF (false positive volume fraction) and TPVF (true positive volume fraction) are defined as follows.

$$FPVF = \frac{|C_O - C_{td}|}{|C_{td}|} \times 100, \quad (4.7)$$

$$TPVF = \frac{|C_O \cap C_{td}|}{|C_{td}|} \times 100. \quad (4.8)$$

FPVF denotes the amount of tissue falsely identified by the method, and TPVF denotes the amount of tissue correctly identified by the method.

Table 2 shows FPVF and TPVF for segmenting WM, GM, and CSF on 20 clinical scene data sets by using  $\kappa$ VSROE. Mean and standard deviation of two factors over the scene population are listed. Table 2 shows that this algorithm agrees with “true” delineation with over 98% TPVF and less than 3% FPVF for the WM and GM objects. The slightly lower TPVF for CSF is due to partial volume spels around the brain parenchyma and the much smaller CSF volume than that of the WM and GM objects compared to the spels affected by the partial volume phenomenon.

Table 2

The mean and standard deviation (in parenthesis) of intra-, inter-operator, and repeat-scan precision, and FPVF, and TPVF for segmenting WM, GM, and CSF over 20 scene data by using the  $\kappa$ VSROE and  $\kappa$ SSROE methods

Method	Precision			Accuracy	
	$PR^{T_1}$	$PR^{T_2}$	$PR^{T_3}$	FPVF	TPVF
$\kappa$ VSROE					
WM	100(0.00)	100(0.00)	97.74(0.82)	2.14(1.02)	98.14(0.62)
GM	100(0.00)	100(0.00)	97.25(0.93)	2.98(0.89)	98.66(0.73)
CSF	100(0.00)	100(0.00)	96.87(1.61)	1.64(0.88)	97.27(1.61)
$\kappa$ SSROE					
WM	100(0.00)	100(0.00)	97.26(0.91)	3.22(1.74)	97.62(1.96)
GM	100(0.00)	100(0.00)	97.67(0.78)	3.41(1.45)	97.32(1.54)
CSF	100(0.00)	100(0.00)	96.54(1.74)	3.78(1.90)	96.76(1.87)

Table 3

The FPVF and TPVF achieved for segmenting WM, GM, and CSF over simulated MRI scene data sets by using the  $\kappa$ VSRFOE method are shown in each cell for different levels of noise and inhomogeneity

Noise		1%		3%		5%		7%	
Inhomo.	Tissue	FPVF	TPVF	FPVF	TPVF	FPVF	TPVF	FPVF	TPVF
0%	WM	3.2	96.4	3.0	93.4	3.8	92.7	5.4	92.4
	GM	5.2	94.8	7.7	95.8	8.3	95.2	8.7	93.9
	CSF	6.1	94.1	5.4	94.2	5.4	94.0	5.7	93.9
20%	WM	2.7	95.6	2.8	92.6	3.7	92.4	5.2	92.2
	GM	5.7	95.3	8.1	95.8	8.5	95.1	8.8	93.9
	CSF	6.5	94.5	5.7	94.4	5.9	94.2	6.3	94.0
40%	WM	2.5	94.7	3.1	93.6	3.9	92.8	5.5	92.5
	GM	6.3	95.9	5.4	95.7	8.3	95.1	8.5	93.8
	CSF	6.1	94.6	5.4	94.0	5.4	93.8	5.7	93.9

Table 3 lists FPVF and TPVF for segmenting WM, GM, and CSF on simulated MRI scene data sets with different levels of noise and inhomogeneity obtained by using  $\kappa$ VSRFOE. We note that all these simulated MRI scene data sets have been first corrected for inhomogeneity by using the method described in [53]. From Table 3, we observe that  $\kappa$ VSRFOE shows an effective performance. It has over 92% TPVF and less than 9% FPVF for each of segmented WM, GM, and CSF. A sample of the segmentation results is presented in Fig. 6.

#### 4.4.3. Efficiency

The proposed algorithm is implemented in the 3DVIEWNIX software system [57] and is executed on an Intel Pentium IV 1.7 GHZ PC under the Red Hat Linux OS kernel version 2.4.7. All timings reported here are with respect to this implementation.

In determining the efficiency of a segmentation method, four types of efficiency factors need to be considered [51]: computer time required for algorithm training and for segmenting each scene, and operator time required for algorithm training and for segmenting each scene. For  $\kappa$ VSRFOE, training is needed only once for an application domain and not for every scene to be segmented. The computer time needed for this training is under 30 s. The average computer time needed for segmenting the three objects in each  $256 \times 256 \times 56$  2-component vectorial scene is 2.5 min. (The average time required for inhomogeneity correction and standardization per scene is 20 and 5 s, respec-

tively.) This algorithm requires about one minute of operator time for algorithm training to estimate parameters, and on the average about 30 s of operator time to specify seed points for different tissues needed for segmenting each scene.

#### 4.5. Comparison

In the previous section, we assessed the performance of algorithm  $\kappa$ VSRFOE in terms of its own precision, accuracy, and efficiency. In this section, we shall compare its performance, again by using these metrics, with that of a scalar version of the relative fuzzy connectedness method that uses some intermediate ad hoc steps to harness the vectorial information [52]. We refer to it as algorithm  $\kappa$ SSRFOE. The basic idea of the  $\kappa$ SSRFOE method is to compute scale in a scalar manner by using one of the scalar component scenes and then the fuzzy affinity for each component of the vectorial scene separately, and then to combine them into a single fuzzy affinity. Other steps are similar to those of  $\kappa$ VSRFOE. In [52], affinity was defined as the minimum of the affinities defined based on the two components of the vectorial scene separately. Our comparison of these two methods will be based on ( $D_1$ ) the 20 clinical data sets utilized in the previous section as well as ( $D_2$ ) a set of 250 mathematical phantoms that were derived from real objects. For  $D_2$ , the phantom scenes were generated from 10 different patient 3D PD-weighted and  $T_2$ -weighted MRI scenes of the brain. One slice of the PD- and

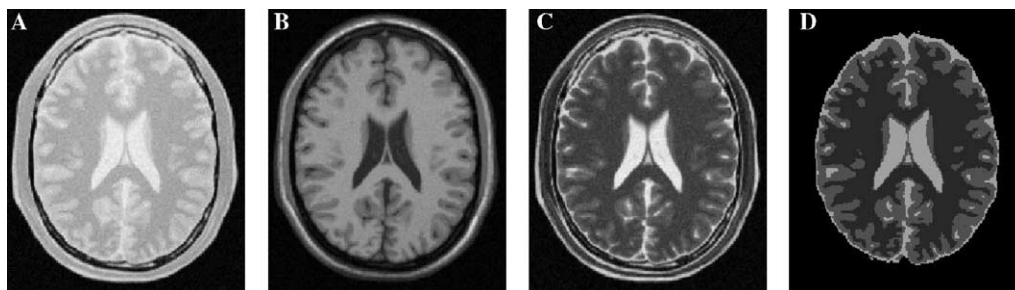


Fig. 6. (A–C) One corresponding slice of PD,  $T_1$ , and  $T_2$ -weighted simulated MRI scenes from the BrainWeb database, with 3% noise and 20% inhomogeneity. (D) Segmented result by using the  $\kappa$ VSRFOE method. Segmented tissues from dark to bright are WM, GM, and CSF.



$T_2$ -weighted MRI scene, approximately at the same location in the brain, was selected from each of these 10 3D scenes. Each of these 10 2D scenes was separated into WM, GM, and CSF by utilizing a user-steered segmentation method [7] on one component ( $T_2$ ) of the 2D scene under the guidance of an expert. The results will be used as true segmentation in our evaluation. Since tracing of peripheral CSF is very ill-defined, only the ventricular part of CSF was taken into account. From this information, from each of the original 10 2D scenes, a new 2D scene was generated by assigning to pixels in each tissue region a constant vector-valued intensity equal to the average of the vectorial intensities within the same segmented tissue region in the corresponding original PD- and  $T_2$ -weighted MR 2D scene. From this set of 10 simulated 2D scenes, we created a total of 250 2D scenes by independently blurring (by using a 2D Gaussian kernel) each component of each 2D scene in this set to five different degrees of blurring and by independently adding to each component of each 2D scene a 0-mean Gaussian correlated noise component at five different levels. Each component of each 2D scene in this set was further modified by adding a fixed slow varying (ramp) background variation that changed from 0 at

the first column to 100 at the last column in the  $256 \times 256$  2D scene. This new set of 2D scenes, denoted  $E = \{C_i = (C, f_i) | 1 \leq i \leq 250\}$ , was used in our experiments. Three examples from this set at different levels of blur and noise are displayed in Figs. 7C–H corresponding to the original scenes shown in Figs. 7A and B. Figs. 8A–C show the segmented results produced by the  $\kappa$ VSRFOE method for the scenes depicted in Figs. 7C–H, respectively. Figs. 9A–C show the segmented results produced by the  $\kappa$ SSRFOE method for the same scenes.

For ( $D_1$ ), Table 2 lists the mean and standard deviation of intra-, inter-operator, and repeat-scan precision, and FPVF, and TPVF for segmenting WM, GM, and CSF over 20 scene data sets by using the  $\kappa$ VSRFOE and  $\kappa$ SSRFOE methods. It can be observed from this table that both  $\kappa$ VSRFOE and  $\kappa$ SSRFOE methods have 100% intra- and inter-operator precision as described in Section 4.4.1, and these two methods have similar repeat-scan precision. As for accuracy, for each of WM, GM, and CSF objects and for each of FPVF and TPVF, a paired  $t$  test of the 20 metric values demonstrates that  $\kappa$ VSRFOE achieves better FPVF and TPVF than  $\kappa$ SSRFOE for all three objects with  $p < 0.001$ . Efficiency is similar for these two methods.

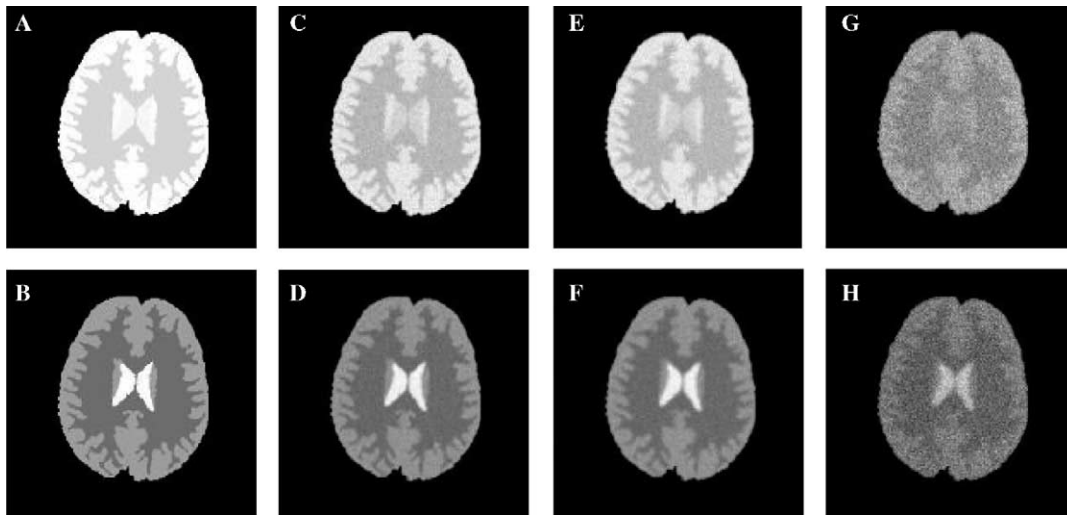


Fig. 7. Three sample 2D vectorial scenes with two components simulated by blurring, adding noise, and adding a background variation to the WM, GM, and CSF regions segmented from patient PD- and  $T_2$ -weighted MRI data sets. (A and B) Original (true) objects; (C and D) Low noise and blurring; (E and F) Medium noise and blurring; (G and H) High noise and blurring. The top and bottom rows show PD- and  $T_2$ -weighted components, respectively.

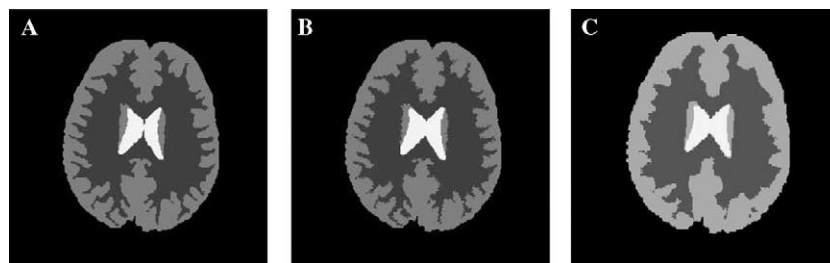


Fig. 8. Results produced by the  $\kappa$ VSRFOE method for the scenes displayed in Fig. 7. (A) For Figs. 7C and D; (B) for Figs. 7E and F; (C) for Figs. 7G and H. Segmented tissues from dark to bright are WM, GM, and CSF.

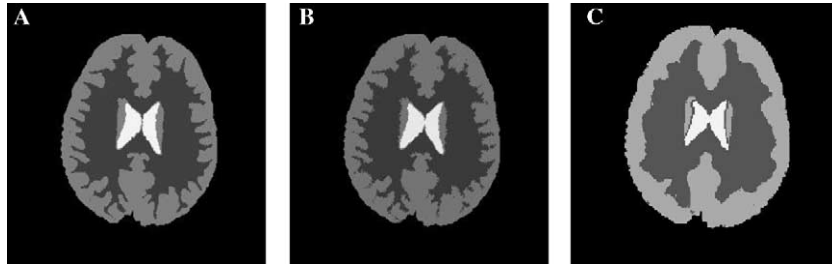


Fig. 9. Results produced by the  $\kappa$ SSRFOE method for the scenes displayed in Fig. 7. (A) For Figs. 7C and D; (B) for Figs. 7E and F; (C) for Figs. 7G and H. Segmented tissues from dark to bright are WM, GM, and CSF.

For ( $D_2$ ), the intra- and inter-operator precisions are identical and efficiency is similar for these two methods. There is no repeat-scan precision available since we did not simulate this. For accuracy, we take the segmented WM as an example to demonstrate in detail the performance behavior of  $\kappa$ VSRFOE with  $\kappa$ SSRFOE. Tables 4 and 5 list in each cell the mean and the standard deviation

of FPVF and TPVF achieved for WM for  $\kappa$ VSRFOE and for  $\kappa$ SSRFOE for each degree of blurring and noise for the 10 scenes in ( $D_2$ ). The degree of blurring and noise increases along columns and rows, respectively. We make the following observations from the tables.  $\kappa$ VSRFOE produces better FPVF than  $\kappa$ SSRFOE. At low levels of noise and blurring, these two methods produce similar TPVF. As

Table 4

The mean and standard deviation (in parenthesis) of FPVF and TPVF achieved for WM by using the  $\kappa$ VSRFOE method are shown in each cell for different blurring and noise conditions

	Noise 1	Noise 2	Noise 3	Noise 4	Noise 5
<i>Blur 1</i>					
FPVF	0.25(0.07)	1.38(0.31)	1.79(0.47)	3.76(1.85)	4.98(2.02)
TPVF	99.27(0.07)	98.54(0.28)	97.92(0.31)	95.08(1.49)	94.77(1.53)
<i>Blur 2</i>					
FPVF	0.82(0.25)	2.36(0.58)	2.43(0.65)	4.68(2.11)	6.39(2.85)
TPVF	99.09(0.13)	97.61(0.16)	97.13(0.48)	94.00(1.62)	93.41(1.71)
<i>Blur 3</i>					
FPVF	1.62(0.69)	2.91(0.72)	3.02(0.89)	5.51(2.31)	7.64(2.91)
TPVF	98.53(0.23)	96.99(0.31)	96.29(0.68)	92.76(1.46)	91.65(1.67)
<i>Blur 4</i>					
FPVF	2.25(0.70)	3.34(0.89)	3.55(1.04)	6.24(2.40)	8.60(3.60)
TPVF	97.78(0.29)	96.34(0.53)	95.58(0.83)	91.78(1.37)	90.63(1.58)
<i>Blur 5</i>					
FPVF	2.84(0.92)	3.81(0.98)	4.10(1.24)	6.95(4.46)	9.69(5.21)
TPVF	97.01(0.36)	95.84(0.67)	94.84(0.83)	91.02(1.15)	89.74(1.47)

Table 5

The mean and standard deviation of FPVF and TPVF achieved for WM by using the  $\kappa$ SSRFOE method are shown in each cell for different blurring and noise conditions

	Noise 1	Noise 2	Noise 3	Noise 4	Noise 5
<i>Blur 1</i>					
FPVF	4.19(1.08)	3.65(1.03)	6.57(2.73)	9.89(2.54)	12.86(3.76)
TPVF	99.68(0.11)	99.11(0.60)	97.34(1.98)	93.24(2.61)	89.56(0.58)
<i>Blur 2</i>					
FPVF	4.47(1.15)	4.20(1.37)	5.99(2.34)	10.52(2.64)	13.90(3.59)
TPVF	99.36(0.40)	98.30(0.79)	95.60(1.72)	90.18(1.12)	88.97(2.75)
<i>Blur 3</i>					
FPVF	4.64(1.41)	4.76(1.56)	6.85(2.61)	11.29(2.80)	14.84(3.56)
TPVF	98.48(0.48)	96.87(0.90)	94.32(1.61)	89.62(0.78)	88.50(2.58)
<i>Blur 4</i>					
FPVF	5.01(1.62)	5.32(1.91)	7.64(2.83)	11.86(2.99)	15.29(3.26)
TPVF	97.47(0.39)	96.17(0.97)	93.33(1.45)	89.33(0.61)	88.11(2.37)
<i>Blur 5</i>					
FPVF	5.38(1.75)	5.87(2.10)	8.44(2.97)	12.24(3.10)	15.79(3.40)
TPVF	96.91(0.37)	95.50(1.03)	92.49(1.25)	89.10(0.54)	87.95(2.47)

Table 6  
Summary of comparison between the  $\kappa$ VSRFOE and  $\kappa$ SSRFOE methods for segmented WM, GM, and CSF

Object	$\kappa$ VSRFOE > $\kappa$ SSRFOE	$\kappa$ SSRFOE > $\kappa$ VSRFOE
<i>WM</i>		
FPVF	22	0
TPVF	20	2
<i>GM</i>		
FPVF	18	3
TPVF	20	1
<i>CSF</i>		
FPVF	0	23
TPVF	21	0

The number of situations out of 25 blur and noise level combinations are shown in each cell where one method fared better than the other.

noise increases,  $\kappa$ VSRFOE achieves better relative performance. This can be seen by examining the entries in each row in Tables 4 and 5. We summarize the comparative results in Table 6 for the segmented WM, GM, and CSF objects. Each cell lists the number of combinations (out of 25 blur and noise combinations) in which a method fared better than the other. A method is considered better under a particular metric for a given level of noise and blur if a paired  $t$  test of the 10 metric values for that level of noise and blur so indicates with a  $p$  value not greater than 0.05. For WM and GM, all those cases wherein  $\kappa$ SSRFOE >  $\kappa$ VSRFOE correspond to low levels of noise and blur. For CSF,  $\kappa$ VSRFOE fares better than  $\kappa$ SSRFOE at most levels of noise and blur as far as TPVF is considered. However,  $\kappa$ VSRFOE seems to yield higher FPVF than  $\kappa$ SSRFOE for most combinations of levels of noise and blur. (The range of the mean and standard deviation of FPVF for  $\kappa$ VSRFOE were 0.55–9.9 and 0.48–4.81. These values for  $\kappa$ SSRFOE were 0–2.04 and 0–1.61.) This emphasizes the need to consider both metrics in assessing the accuracy of segmentation methods.

## 5. Concluding remarks

In this paper, we have extended our previous framework of fuzzy connectedness from a scalar scene domain to an arbitrary dimensional vectorial scene domain. We have devised fuzzy affinity in a fully vectorial manner, and the estimation of scale has also been done in a vectorial fashion. The previous relative fuzzy connectedness algorithm for multiple objects has been utilized in this development. In addition, we have devised methods to estimate parameters of the various components of the affinity relation in a manner different from that employed previously.

We have presented several studies to evaluate the performance of the new method based on simulated and clinical MRI scenes. For the simulated MRI scenes with different levels of noise and inhomogeneity, the results indicate that the method has an effective accuracy performance. It achieves over 92% TPVF and less than 9% FPVF. For clinical MRI scenes for segmenting the com-

ponent brain tissues, the method has 100% inter- and intra-operator precision, and about 97% repeat-scan precision for WM, GM, and CSF objects. The method has an accuracy characterized by over 97% TPVF and less than 3% FPVF for WM, GM, and CSF objects. In terms of efficiency, the method needs a one-time training for an application domain and not for every scene to be segmented. The training step requires less than one minute of operator time and 30 s of computer time to estimate parameters, and the average computer time needed for segmenting three objects in a  $256 \times 256 \times 56$  2-component vectorial scene is about 2.5 min on a 1.7 GHZ Pentium IV PC running under Red Hat Linux OS kernel version 2.4.7. Based on 20 clinical MRI scenes and 250 phantom scenes generated under a range of conditions of blurring, noise, and background variation, a quantitative comparison between the new method and the method that uses some intermediate ad hoc steps to fit the vectorial scene to a scalar fuzzy connectedness formulation indicates that these two methods have similar precision and efficiency, but the vectorial method has overall better accuracy. We are in the process of carefully assessing the improvements in segmentation that may result from these new methods in our various ongoing applications.

Instead of using just intensity only for defining  $\phi_{vs}$ , other intensity-based features may also be used. In addition, in current fuzzy affinity construction, we combine homogeneity-based and object-feature-based components of affinity in a fixed manner; see (2.14). The weight for these two components may be varied within the scene in an adaptive manner along the lines suggested in [58].

In [41], we described an iterative relative fuzzy connectedness framework for the scalar case and proved its robustness in practical scene segmentation. The fully vectorial relative fuzzy connectedness formulation presented in this paper can also be extended to the iterative relative version which may further improve the segmentation performance.

Finally, one drawback of vectorial relative fuzzy connectedness as formulated presently is that the affinity used for the different objects must be the same. This restriction somewhat compromises the effectiveness of the segmentation that can be achieved. We are currently investigating the theoretical, algorithmic, and application aspects of using different affinities for different objects in vectorial relative and iterative relative fuzzy connectedness.

## Acknowledgment

The research reported here is supported by a US DHHS Grant NS 37172.

## Appendix A

Proofs of the new results stated in the body of the paper are given in this appendix.

Proof of Proposition 1.

**Proof.** For any  $c = d$  in  $C$ , in (2.9),  $\mathbf{f}(e) - \mathbf{f}(e') = \mathbf{0}$ , and  $W_h(\mathbf{f}(e) - \mathbf{f}(e')) = 1$  from (2.6). Therefore,  $\mathbf{D}(c, d) = \mathbf{0}$  in (2.9), and  $\mu_{\psi_{ts}}(c, d) = 1$  in (2.10), proving the reflexivity of  $\psi_{ts}$ .  $\square$

In (2.10),  $\|e - c\| = \|e' - d\|$  and  $B_{cd}(c) = B_{dc}(d)$ . Hence, the denominator in (2.10) does not change by interchanging the roles of  $c$  and  $d$ . Therefore, to prove the symmetry of  $\psi_{ts}$ , it is enough to show that  $|\mathbf{D}(c, d)| = |\mathbf{D}(d, c)|$  for any  $c, d \in C$ . In (2.9),  $\mathbf{f}(e) - \mathbf{f}(e') = -(\mathbf{f}(e') - \mathbf{f}(e))$ , and  $W_h(\mathbf{f}(e) - \mathbf{f}(e')) = W_h(\mathbf{f}(e') - \mathbf{f}(e))$  from (2.6). Then

$$\begin{aligned} \mathbf{D}(c, d) &= \sum_{\substack{e \in B_{cd}(c) \\ e' \in B_{cd}(d) \\ e-e'=c-d}} (1 - W_h(\mathbf{f}(e) - \mathbf{f}(e'))) \omega_{cd}(\|e - c\|) \frac{\mathbf{f}(e) - \mathbf{f}(e')}{|\mathbf{f}(e) - \mathbf{f}(e')|} \\ &= \sum_{\substack{e' \in B_{dc}(d) \\ e \in B_{dc}(c) \\ e'-e=d-c}} (1 - W_h(\mathbf{f}(e') - \mathbf{f}(e))) \omega_{cd}(\|e' - d\|) \frac{-(\mathbf{f}(e') - \mathbf{f}(e))}{|\mathbf{f}(e') - \mathbf{f}(e)|} \\ &= -\mathbf{D}(d, c). \end{aligned}$$

Therefore,  $|\mathbf{D}(c, d)| = |\mathbf{D}(d, c)|$ .

$\phi_{ts}$  is reflexive by definition (2.12). Also, from (2.12),  $\mu_{\phi_{ts}}(c, d) = \mu_{\phi_{ts}}(d, c)$  for any  $c, d \in C$ , and so  $\phi_{ts}$  is symmetric.

Since  $\alpha, \psi_{ts}, \phi_{ts}$  are reflexive, from (2.14) it readily follows that  $\kappa$  is reflexive.

Also, Since  $\alpha, \psi_{ts}, \phi_{ts}$  are symmetric, it is easily verified in (2.14) that  $\mu_{\kappa}(c, d) = \mu_{\kappa}(d, c)$  for any  $c, d \in C$ . Hence,  $\kappa$  is a legitimate fuzzy spel affinity in  $C$ .

Proof of Theorem 2.

**Proof.** Let  $\mathcal{N}_{\kappa}$  be the fuzzy  $\kappa$ -net of  $C$ . For any spel  $c \in C$ ,  $\mu_{\kappa}(c, c) = \max_{p_{cc} \in P_{cc}} [\mu_{\mathcal{N}_{\kappa}}(p_{cc})] = 1$ . So  $K$  is reflexive.  $\square$

For any spels  $c, d \in C$ , we first observe that there is a one-to-one correspondence between  $P_{cd}$  and  $P_{dc}$  as follows: If  $p_{cd} = \langle c = c_1, c_2, \dots, c_q = d \rangle \in P_{cd}$ , then the corresponding element of  $P_{dc}$  is  $p_{dc} = \langle d = c_q, c_{q-1}, \dots, c_1 = c \rangle$ . From the symmetry of  $\kappa$ , clearly,  $\mu_{\mathcal{N}_{\kappa}}(p_{cd}) = \mu_{\mathcal{N}_{\kappa}}(p_{dc})$ . Therefore, by (2.15),  $\mu_{\kappa}(c, d) = \max_{p_{cd} \in P_{cd}} [\mu_{\mathcal{N}_{\kappa}}(p_{cd})] = \max_{p_{dc} \in P_{dc}} [\mu_{\mathcal{N}_{\kappa}}(p_{dc})] = \mu_{\kappa}(d, c)$ . Hence,  $K$  is symmetric.

For any spels  $c, e \in C$ , we know  $P_{ce} = \{p_{cd} + p_{de} | d \in C \text{ and } p_{cd} \in P_{cd} \text{ and } p_{de} \in P_{de}\}$  (by Proposition 2.1 in [38]). Therefore,

$$\begin{aligned} \mu_{\kappa}(c, e) &= \max_{p_{ce} \in P_{ce}} [\mu_{\mathcal{N}_{\kappa}}(p_{ce})], \text{ by (2.15)} \\ &= \max_{\substack{p_{cd} \in P_{cd} \\ p_{de} \in P_{de}}} \text{getmathopsub } d \in C [\mu_{\mathcal{N}_{\kappa}}(p_{cd} + p_{de})] \\ &= \max_{d \in C} [\max_{p_{cd} \in P_{cd}} [\max_{p_{de} \in P_{de}} [\min(\mu_{\mathcal{N}_{\kappa}}(p_{cd}), \mu_{\mathcal{N}_{\kappa}}(p_{de}))]]] \\ &= \max_{d \in C} [\max_{p_{cd} \in P_{cd}} [\min[\max_{p_{de} \in P_{de}} (\mu_{\mathcal{N}_{\kappa}}(p_{de}), \mu_{\mathcal{N}_{\kappa}}(p_{cd}))]]] \\ &= \max_{d \in C} [\min[\max_{p_{cd} \in P_{cd}} (\mu_{\mathcal{N}_{\kappa}}(p_{cd})), \max_{p_{de} \in P_{de}} (\mu_{\mathcal{N}_{\kappa}}(p_{de}))]] \\ &= \max_{d \in C} [\min(\mu_{\kappa}(c, d), \mu_{\kappa}(d, e))], \text{ by (2.15)}. \end{aligned}$$

Hence  $K$  is transitive. Thus,  $K$  is reflexive, symmetric, and transitive.

Proof of Theorem 3.

**Proof.** Let  $\Omega$  denote the set on the right-hand side of (2.21). By (2.17) and (2.20), each spel  $s \in S$  is in the set  $O_{K\theta}(S)$ . Let  $c \in O_{K\theta}(S)$ . By (2.18) and (2.20),  $\max_{s \in S} [\mu_{\kappa}(s, c)] \geq \theta$ . Hence,  $c \in \Omega$  and  $O_{K\theta}(S) \subset \Omega$ . To prove  $\Omega \subset O_{K\theta}(S)$ , we take any spel  $c \notin O_{K\theta}(S)$ . By (2.19) and (2.20),  $\max_{s \in S} [\mu_{\kappa}(s, c)] < \theta$ . Hence,  $c \notin \Omega$  and  $\Omega \subset O_{K\theta}(S)$ . Therefore,  $\Omega = O_{K\theta}(S)$ .  $\square$

## References

- [1] Z.H. Cho, J.P. Jones, M. Sing, Foundation of Medical Imaging, John Wiley, New York, 1993.
- [2] N.R. Pal, S.K. Pal, A review of image segmentation techniques, Pattern Recognition 26 (9) (1993) 1277–1294.
- [3] D. Morgenthaler, A. Rosenfeld, Multidimensional edge detection by hypersurface fitting, IEEE Trans. Pattern Anal. Mach. Intell. 3 (4) (1981) 482–486.
- [4] M. Kass, A. Witkin, D. Terzopoulos, Snakes: active contour models, Int. J. Comput. Vis. 1 (4) (1987) 321–331.
- [5] T. McInerney, D. Terzopoulos, Deformable models in medical image analysis: a survey, Med. Image Anal. 1 (2) (1996) 91–108.
- [6] G. Sapiro, Color snakes, Comput. Vis. Image Understand. 68 (2) (1997) 247–253.
- [7] A.X. Falcão, J.K. Udupa, S. Samarasekera, S. Sharma, B.E. Hirsch, R.A. Lotufo, User-steered image segmentation paradigms: live wire and live lane, Graph. Models Image Process. 60 (4) (1998) 233–260.
- [8] E. Mortensen, W. Barrett, Intelligent scissors for image composition, in: Proc. SIGGRAPH'95, Los Angeles, USA, 1995, pp. 191–198.
- [9] T. Cootes, C. Taylor, D. Cooper, Active shape models-their training and application, Comput. Vis. Image Understand. 61 (1) (1995) 38–59.
- [10] T. Cootes, G. Edwards, C. Taylor, Active appearance models, IEEE Trans. Pattern Anal. Mach. Intell. 23 (6) (2001) 681–685.
- [11] J. Sethian, Level Set Methods and Fast Marching Methods, Cambridge University Press, Cambridge, 1996.
- [12] N. Otsu, A threshold selection method from gray-level histogram, IEEE Trans. Systems, Man Cybernet. 9 (1) (1979) 62–66.
- [13] A.K.C. Wong, P.K. Sahoo, A gray-level threshold selection method based on maximum entropy principle, IEEE Trans. Systems, Man, Cybernet. 19 (4) (1989) 866–871.
- [14] Y. Chang, X. Li, Adaptive image region-growing, IEEE Trans. Image Process. 3 (6) (1994) 868–872.
- [15] T. Cover, P. Hart, Nearest neighbor pattern classification, IEEE Trans. Informat. Theory 13 (1) (1967) 21–27.
- [16] R. Duda, P. Hart, Pattern Classification and Scene Analysis, John Wiley, New York, 1973.
- [17] M. Trivedi, J. Bezdek, Low-level segmentation of aerial images with fuzzy clustering, IEEE Trans. Systems, Man, Cybernet. 16 (4) (1986) 589–598.
- [18] Y.W. Lim, S.U. Lee, On the color image segmentation algorithm based on the thresholding and the fuzzy c-means technique, Pattern Recognit. 23 (9) (1990) 935–952.
- [19] Y. Boykov, O. Veksler, R. Zabih, Fast approximate energy minimization via graph cuts, IEEE Trans. Pattern Anal. Mach. Intell. 23 (11) (2001) 1222–1239.
- [20] Z. Wu, R. Leahy, An optimal graph theoretic approach to data clustering: theory and its application to image segmentation, IEEE Trans. Pattern Anal. Mach. Intell. 15 (11) (1993) 1101–1113.
- [21] J.L. Marroquin, B.C. Vemuri, S. Botello, F. Calderon, A. Fernandez-Bouzas, An accurate and efficient Bayesian method for automatic segmentation of brain MRI, IEEE Trans. Med. Imag. 21 (8) (2002) 934–945.



- [22] S.Z. Li, Markov Random Field Modeling in Computer vision, Springer-Verlag, Berlin, Germany, 1995.
- [23] Y. Zhang, M. Brady, S. Smith, Segmentation of brain MR images through a hidden Markov random field model and the expectation-maximization algorithm, *IEEE Trans. Med. Imag.* 20 (1) (2001) 45–57.
- [24] K. Held, E.R. Kopsa, B.J. Krause, W.M. Wells, R. Kikinis, H.W. Muller-Gartner, Markov random field segmentation of brain MR images, *IEEE Trans. Med. Imag.* 16 (6) (1997) 878–886.
- [25] J.C. Rajapakse, F. Kruggel, Segmentation of MR images with intensity inhomogeneities, *Image Vis. Comput.* 16 (1998) 165–180.
- [26] Z. Kato, Bayesian color image segmentation using reversible jump Markov chain Monte Carlo, *CWI Research Report PNA-R9902*, ISSN 1386-3711, 1999.
- [27] S. Beucher, F. Meyer, The morphological approach to segmentation: The watershed transformation, in: *Mathematical Morphology in Image Processing*, vol. 12, Marcel Dekker, USA, 1993, pp. 433–481.
- [28] I. Vanhamel, I. Pratikakis, H. Sahli, Multiscale gradient watersheds of color images, *IEEE Trans. Image Process.* 12 (6) (2003) 617–626.
- [29] C. Chu, J. Aggarwal, The integration of image segmentation maps using region and edge information, *IEEE Trans. Pattern Anal. Mach. Intell.* 15 (12) (1993) 1241–1252.
- [30] A. Chakraborty, L. Staib, J. Duncan, Deformable boundary finding in medical images by integrating gradient and region information, *IEEE Trans. Med. Imag.* 15 (6) (1996) 859–870.
- [31] T. Jones, D.N. Metaxas, Automated 3D segmentation using deformable models and fuzzy affinity, in: *Proc. Information Processing in Medical Imaging*, Poultny, USA, 1997, pp. 113–126.
- [32] C. Imielinska, D. Metaxas, J.K. Udupa, Y. Jin, T. Chen, Hybrid segmentation of anatomical data, in: *Proc. MICCAI*, vol. 2208, Utrecht, The Netherlands, 2001, pp. 1048–1057.
- [33] S.C. Zhu, A. Yuille, Region competition: unifying snakes, region growing, and Bayes/MDL for multiband image segmentation, *IEEE Trans. Pattern Anal. Mach. Intell.* 18 (9) (1996) 884–900.
- [34] J.C. Bezdek, S.K. Pal, *Fuzzy Models for Pattern Recognition*, IEEE Press, New York, 1992.
- [35] A. Kaufmann, *Introduction to the Theory of Fuzzy Subsets*, vol. 1, Academic Press, New York, 1975.
- [36] A. Rosenfeld, Fuzzy digital topology, *Informat. Control* 40 (1) (1979) 76–87.
- [37] I. Bloch, Fuzzy connectivity and mathematical morphology, *Pattern Recognit. Lett.* 14 (1) (1993) 483–488.
- [38] J.K. Udupa, S. Samarasekera, Fuzzy connectedness and object definition: theory, algorithms, and applications in image segmentation, *Graph. Models Image Process.* 58 (3) (1996) 246–261.
- [39] P.K. Saha, J.K. Udupa, D. Odhner, Scale-based fuzzy connected image segmentation: theory, algorithms, and validation, *Comput. Vis. Image Understand.* 77 (9) (2000) 145–174.
- [40] P.K. Saha, J.K. Udupa, Relative fuzzy connectedness among multiple objects: theory, algorithms, and applications in image segmentation, *Comput. Vis. Image Understand.* 82 (1) (2001) 42–56.
- [41] J.K. Udupa, P.K. Saha, R.A. Lotufo, Relative fuzzy connectedness and object definition: theory, algorithms, and applications in image segmentation, *IEEE Trans. Pattern Anal. Mach. Intell.* 24 (11) (2002) 1485–1500.
- [42] G.T. Herman, B.M. Carvalho, Multiseeded segmentation using fuzzy connectedness, *IEEE Trans. Pattern Anal. Mach. Intell.* 23 (5) (2001) 460–474.
- [43] L.G. Nyúl, A.X. Falcão, J.K. Udupa, Fuzzy-connected 3D image segmentation at interactive speeds, *Graph. Models* 64 (5) (2003) 259–281.
- [44] P.K. Saha, J.K. Udupa, Fuzzy connected object delineation: axiomatic path strength definition and the case of multiple seeds, *Comput. Vis. Image Understand.* 83 (3) (2001) 275–295.
- [45] J.K. Udupa, L. Wei, S. Samarasekera, Y. Miki, M.A. Buchem, R.I. Grossman, Multiple sclerosis lesion quantification using fuzzy connectedness principles, *IEEE Trans. Med. Imag.* 16 (5) (1997) 598–609.
- [46] J. Liu, J.K. Udupa, D. Odhner, J.M. McDonough, R. Arens, System for upper airway segmentation and measurement with MR imaging and fuzzy connectedness, *Acad. Radiol.* 10 (1) (2003) 13–24.
- [47] T. Lei, J.K. Udupa, P.K. Saha, D. Odhner, Artery–vein separation via MRA—an image processing approach, *IEEE Trans. Med. Imag.* 20 (8) (2001) 689–703.
- [48] P.K. Saha, J.K. Udupa, E.F. Conant, D.P. Chakraborty, D. Sullivan, Breast tissue density quantification via digitized mammograms, *IEEE Trans. Med. Imag.* 20 (8) (2001) 792–803.
- [49] G. Moonis, J. Liu, J.K. Udupa, D. Hackney, Estimation of tumor volume using fuzzy connectedness segmentation of MRI, *Am. J. Neuroradiol.* 23 (3) (2002) 356–363.
- [50] Z. Liang, J.R. MacFall, D.P. Harrington, Parameter estimation and tissue segmentation from multispectral MR images, *IEEE Trans. Med. Imag.* 13 (3) (1994) 441–449.
- [51] J.K. Udupa, V.R. LeBlanc, H. Schmidt, C. Imielinska, P.K. Saha, G.J. Grevera, Y. Zhuge, L.M. Currie, P. Molholt, Y. Jin, Methodology for evaluating image segmentation algorithms, in: *Proc. SPIE Medical Imaging*, vol. 4684, San Diego, USA, 2002, pp. 266–277.
- [52] L.G. Nyúl, J.K. Udupa, A protocol-independent brain MRI segmentation method, in: *Proc. SPIE Medical Imaging*, vol. 4684, San Diego, USA, 2002, pp. 1588–1599.
- [53] Y. Zhuge, J.K. Udupa, J. Liu, P.K. Saha, T. Iwanaga, A scale-based method for correcting background intensity variation in acquired images, in: *Proc. SPIE Medical Imaging*, vol. 4684, San Diego, USA, 2002, pp. 1103–1111.
- [54] M. Styner, C. Brechbuhler, G. Szekely, G. Gerig, Parametric estimate of intensity inhomogeneities applied to MRI, *IEEE Trans. Med. Imag.* 19 (3) (2000) 153–165.
- [55] D.L. Collins, A.P. Zijdenbos, V. Kollokian, J.G. Sled, N.J. Kabani, C.J. Holmes, A.C. Evans, Design and construction of a realistic digital brain phantom, *IEEE Trans. Med. Imag.* 17 (3) (1998) 463–468.
- [56] L.G. Nyúl, J.K. Udupa, On standardizing the MR image intensity scale, *Magn. Reson. Med.* 42 (6) (1999) 1072–1081.
- [57] J.K. Udupa, D. Odhner, S. Samarasekera, R.J. Goncalves, K. Iyer, K. Venugopal, S. Furuie, 3DVIEWNIX: an open, transportable, multidimensional multimodality, multiparametric imaging software system, in: *Proc. SPIE Medical Imaging*, vol. 2164, Newport Beach, USA, 1994, pp. 58–73 (Also downloadable from [www.mipg.uenn.edu](http://www.mipg.uenn.edu)).
- [58] A.S. Pednekar, I.A. Kakadiaris, Adaptive fuzzy connectedness-based medical image segmentation, in: *Proc. Indian Conf. on Computer Vision, Graphics, and Image Processing*, Ahmadabad, India, 2003, pp. 457–462.